Separation and Purification Technology 387 (2026) 136692

Contents lists available at ScienceDirect

Separation and Purification Technology

journal homepage: www.elsevier.com/locate/seppur

Strategic molecular engineering of ultrastable porous organic polymer engineered with tetraethynylpyrene-functionalized benzoxazine for superior CO_2 capture via solid-state chemical conversion

Mohamed Gamal Mohamed [a,b,1], Yang-Chin Kao [a,1], Bo-Xuan Su [a], Hira Karim [c], Shiao-Wei Kuo [a,d,*]

[a] Department of Materials and Optoelectronic Science, Center for Functional Polymers and Supramolecular Materials, National Sun Yat-Sen University, Kaohsiung 804, Taiwan
[b] Department of Chemistry, Faculty of Science, Assiut University, Assiut 71516, Egypt
[c] Department of Chemistry, School of Natural Sciences (SNS), National University of Sciences and Technology (NUST), H-12, Islamabad 44000, Pakistan
[d] Department of Medicinal and Applied Chemistry, Kaohsiung Medical University, Kaohsiung 807, Taiwan

ARTICLE INFO

Editor name: Dr. S Shouliang Yi

Keywords:
Tetraethynylpyrene
Benzoxazine
Polybenzoxazine
Porous organic polymers
Solid-state chemical conversion
CO_2 uptake

ABSTRACT

Rapid industrialization and population growth have increased energy demand, accelerating CO_2 emissions and intensifying climate-related challenges. To address these challenges, researchers are developing advanced carbon capture technologies to mitigate atmospheric CO_2 and its associated environmental impacts. Therefore, we report herein the design, synthesis, and comprehensive characterization of a tetraethynylpyrene-based benzoxazine monomer (Pyr-BZ-4Br) and its corresponding porous organic polymer (Pyr-BZ-Pyr POP), constructed via Sonogashira coupling. The Pyr-BZ-4Br monomer was synthesized through a three-step sequence involving Schiff-base condensation, reductive amination, and Mannich ring closure. Thermal analyses [Fourier-transform infrared spectroscopy (FTIR), and differential scanning calorimetry (DSC)] confirmed complete ring-opening of the oxazine above 250 °C, forming a highly crosslinked poly(Pyr-BZ-4Br) network. The Pyr-BZ-Pyr POP displayed a micro/mesoporous architecture with a BET surface area of 117 $m^2\ g^{-1}$, which decreased to 89 $m^2\ g^{-1}$ after thermal curing due to polymerization of the Pyr-BZ-Pyr POP framework into the crosslinked poly(Pyr-BZ-Pyr POP) network. Notably, the CO_2 adsorption capacity increased significantly after thermal curing (1.89 mmol g^{-1} at 273 K) compared to the uncured Pyr-BZ-Pyr POP (0.4 mmol g^{-1}), owing to optimized pore structure and the generation of phenolic -OH groups that enhance host–guest hydrogen bonding.

1. Introduction

The accelerating rise in atmospheric greenhouse gases, particularly carbon dioxide (CO_2), has intensified the demand for materials capable of efficiently capturing and sequestering carbon while remaining compatible with large-scale deployment [1–5]. Conventional strategies—ranging from amine scrubbing to membrane separation—often suffer from high energy penalties, limited selectivity, and poor long-term stability, especially when applied to dilute or mixed gas streams. Consequently, porous solid adsorbents that combine high uptake capacity, tunable pore architectures, and robust chemical stability have attracted sustained interest as practical solutions for point-source carbon capture and decentralized mitigation technologies [6–10]. To address this, several capture methods have been explored, including cryogenic distillation, membrane separation, physical adsorption, and chemical scrubbing techniques. A wide range of solid materials is currently employed for CO_2 capture, including mesoporous silica (MS) [11,12], zeolites [13], metal–organic frameworks (MOFs) [14], clays [15], porous carbon materials (PCMs) [16], POPs [17], and organic–inorganic hybrid compounds [18]. These porous adsorbents interact with CO_2 molecules through different physicochemical mechanisms, depending on their structural and chemical characteristics.

Covalent triazine frameworks (CTFs) [19], covalent organic frameworks (COFs) [20], conjugated microporous polymers (CMPs) [21,22],

* Corresponding author at: Department of Materials and Optoelectronic Science, Center for Functional Polymers and Supramolecular Materials, National Sun Yat-Sen University, Kaohsiung 804, Taiwan.
E-mail address: kuosw@faculty.nsysu.edu.tw (S.-W. Kuo).
[1] These two authors contributed equally.

https://doi.org/10.1016/j.seppur.2025.136692
Received 4 August 2025; Received in revised form 10 December 2025; Accepted 27 December 2025
Available online 28 December 2025

and hypercrosslinked polymers (HPPs) [23], are representative classes of POPs, renowned for their exceptionally high surface area, robust chemical stability, low density, and tunable architectures. Among these materials, porous organic polymers (POPs) have emerged as one of the most promising candidates owing to their permanent nanoscale porosity, structural versatility, and chemical robustness. Unlike inorganic sorbents, POPs are composed mainly of light elements (C, H, N, O) connected through strong covalent linkages, resulting in low density, high thermal stability, and broad functional tunability [24,25]. A wide array of synthetic methodologies has been developed for the preparation of POPs, including Suzuki-Miyaura coupling, Friedel–Crafts alkylation, Buchwald-Hartwig coupling and Schiff-base condensation, Sonogashira–Hagihara cross-coupling, and Mannich condensation, enabling precise control of pore size, surface chemistry, and framework topology. Importantly, recent studies have shown that synthetic strategy and functionality critically govern CO_2 adsorption performance [26,27].

Polybenzoxazines (PBZs), a class of high-performance phenolic thermosetting resins, are typically synthesized via the cationic ring-opening polymerization of benzoxazine monomers, resulting in a densely crosslinked network bridged by tertiary amine linkages [28–37]. These resins can be readily produced from cost-effective starting materials such as primary amines, phenolic compounds, and formaldehyde [38–45]. PBZs exhibit a unique combination of advanced properties that distinguish them from conventional polymers, including exceptionally low water absorption, minimal curing shrinkage, outstanding mechanical strength, high char yield, excellent thermal stability, and superior resistance to chemicals, electricity, and fire [46–54]. Owing to these remarkable characteristics, PBZs are well-suited for a broad range of demanding applications, particularly in electronics, aerospace, CO_2 capture, and water purification technologies [18,55–60]. Several groups have modified POPs through solid-state transformations by adding functional groups such as amine, amide, oxazole, and thiazole [61–64]. In our previous study, we prepared a 3D TPM-BZ-Py POP with a surface area around 185 $m^2\ g^{-1}$ and CO_2 uptake around 0.60 mmol g^{-1} [17], and further developed porous benzoxazine networks (surface area: >320 $m^2\ g^{-1}$, CO_2 uptake: >1.80 mmol g^{-1}) by linking brominated benzoxazine units with ethynyl-functionalized linkers via the Sonogashira–Hagihara method [65]. Tan et al. synthesized POPs with surface areas over 230 $m^2\ g^{-1}$ and CO_2 uptake over 4.0 wt% via a one-step Mannich reaction using triphenols, formaldehyde, and amine [66]. Ma et al. later integrated imine COFs with reduction and Mannich reactions to obtain benzoxazine COFs exceeding 640 $m^2\ g^{-1}$ and CO_2 uptake over 15.0 $cm^3\ g^{-1}$ [67]. To the best of our knowledge, the synthesis and thermal behavior of tetraethynylpyrene-functionalized BZ, along with its corresponding POP, and the application of this POP in gas adsorption, have not yet been reported by other research groups.

We report a convergent strategy to access a Pyr-BZ-4Br and its crosslinked POP (Pyr-BZ-Pyr) via Schiff-base condensation, reductive amination, Mannich condensation, and Sonogashira coupling. The inclusion of a 4-bromosalicylaldehyde “handle” enables efficient thermal ring-opening polymerization (ROP) to generate phenolic -OH sites and an extended hydrogen-bonding network, as confirmed by FTIR, DSC, and TGA. The Pyr-BZ-4Br monomer shows a thermal decomposition temperature (T_{d10}) of 359 °C and a char yield of 53.4 wt% without heat treatment. After undergoing ROP at 280 °C, T_{d10} increases to 466 °C and the char yield rises to 65.6 wt%, confirming the formation of a highly crosslinked poly(Pyr-BZ-4Br) network. The Brunauer–Emmett–Teller (BET) surface area was determined to be 117 $m^2\ g^{-1}$ for the as-synthesized Pyr-BZ-Pyr POP and 89 $m^2\ g^{-1}$ for its thermally cured counterpart, poly(Pyr-BZ-Pyr POP). Notably, CO_2 adsorption capacity significantly increased following thermal curing, reaching 1.89 mmol g^{-1} at 273 K [poly(Pyr-BZ-Pyr POP)], compared to 0.4 mmol g^{-1} for the uncured Pyr-BZ-Pyr POP.

2. Experimental section

2.1. Materials

Sodium borohydride ($NaBH_4$), triphenylphosphine (PPh_3), 1,4-dioxane, and pyrene (Pyr) were purchased from Thermo Scientific. Sodium hydroxide (NaOH), absolute ethanol (EtOH), methanol (MeOH), *N,N*-dimethylformamide (DMF), toluene, 4-ethynylaniline, tetrakis(triphenylphosphine)palladium(0) [$Pd(PPh_3)_4$], anhydrous magnesium sulfate ($MgSO_4$), copper(I) iodide (CuI), nitrobenzene, tetrahydrofuran (THF) and trimethylsilylacetylene were obtained from Sigma-Aldrich. Paraformaldehyde was obtained from Acros Organics. *N,N*-Diethylethanamine (Et_3N) was sourced from Merck. Bromine (Br_2) solution and 4-bromosalicylaldehyde were supplied by Alfa Aesar. Potassium carbonate (K_2CO_3) was obtained from SHOWA, while aluminum oxide (Al_2O_3) was purchased from MACHEREY-NAGEL. Single-walled carbon nanotubes (SWCNTs) with diameters less than 2 nm and lengths ranging from 5 to 15 μm were obtained from Centron Biochemistry Technology, Taiwan.

2.2. Synthesis of 1,3,6,8-tetraethynylpyrene (Pyr-T)

Using a 100 mL round-bottomed vessel, Pyr (1.00 g, 4.94 mmol) was dissolved in nitrobenzene (50 mL), and Br_2 solution (1.20 mL, 22.24 mmol) was added dropwise with stirring, and the reaction mixture was heated to 120 °C for 4 h to obtain Pyr-4Br as a pale-green solid [Yield: 97 %]. In a nitrogen-filled flask, CuI (20 mg), Pyr-4Br (1.00 g, 1.93 mmol), $Pd(PPh_3)_4$ (19 mg), triphenylphosphine (13 mg, 0.05 mmol), and were combined with anhydrous toluene (50 mL) and Et_3N (20 mL). Then trimethylsilylacetylene (1.20 mL, 8.69 mmol) was added in one portion after heating the reaction mixture to 50 °C and keeping the reaction for 48 h at 85 °C. Upon completion, solvents were removed under reduced pressure to yield Pyr-TMS as an orange powder. Pyr-TMS and potassium carbonate (K_2CO_3, 1.33 g, 9.62 mmol) were dissolved in anhydrous MeOH (100 mL) and stirred for 48 h. The resulting reddish-brown solid was recovered by filtration, washed with MeOH, and then purified by column chromatography on Al_2O_3 (eluent: THF) to give Pyr-T as a satuma-colored powder [Yield: 93 %]. FTIR [cm^{-1}]: 3279 (terminal alkyne), 2098 (C≡C). ^{1}H NMR [500 MHz, ppm, δ, $CHCl_3$-*d*, **Fig. S1**]: 8.68, 8.37, and 3.66 (terminal alkyne). ^{13}C NMR [125 MHz, ppm, δ, $CHCl_3$-*d*, **Fig. S2**]: 134.9, 132.5, 127.1, 117.8, 83.8 (pH-**C** ≡ CH) and 81.3 (pH-C ≡ **C**H); ^{1}H NMR [500 MHz, ppm, δ, DMSO-d_6, **Fig. S3**]: 8.63, 8.38, and 4.96 (terminal alkyne). ^{13}C NMR [125 MHz, ppm, δ, DMSO-d_6]: 134.2, 131.5, 126.9, 122.8, 117.8, 88.2 (pH-**C** ≡ CH) and 80.7 (pH-C ≡ **C**H).

2.3. Synthesis of Pyr-T-4NH$_2$

A mixture of Pyr-4Br (1.00 g, 1.93 mmol), 0.90 g (7.72 mmol) 4-ethynylaniline, 0.08 g $Pd(PPh_3)_4$, and 0.01 g CuI was mixed until fully dissolved in 50 mL DMF and 10 mL Et_3N, then heated at 120 °C under N_2 for 24 h. The reaction was poured into ice-cold water, and the precipitated solid was recovered through filtration. Purification by column chromatography on Al_2O_3 (eluent: THF) delivered 1.16 g of Pyr-T-4NH_2 as a burnt-orange solid [Yield: 91 %] [68,69]. FTIR [cm^{-1}]: 3461, 3363 (NH_2), 3030 (sp^2 C—H), and 2191 (C≡C). ^{1}H NMR [500 MHz, ppm, δ, DMSO-d_6]: 8.67, 8.25, 7.46, 6.66, 5.73 (NH_2). ^{13}C NMR [125 MHz, ppm, δ, DMSO-d_6]: 150.0 (aromatic C—N), 133.0, 131.7, 129.9, 126.2, 123.7, 119.2, 113.7, 107.8, 98.8 (Pyr-C ≡ **C**-An) and 85.0 (Pyr-**C** ≡ C-An).

2.4. Synthesis of Pyr-BZ-4Br

Pyr-T-4NH_2 (0.50 g, 0.75 mmol) was dissolved in 50 mL absolute EtOH along with 0.60 g (3.01 mmol) 4-bromosalicylaldehyde. The solution was refluxed for 24 h at 80 °C. The rose-red precipitate was filtered, washed with water, and kept under vacuum to give Pyr-SF-4Br

[78 % yield]. Pyr-SF-4Br (0.80 g, 0.57 mmol) was suspended in 50 mL EtOH, and 0.22 g (5.73 mmol) $NaBH_4$ was gradually introduced, and the reaction mixture was kept under stirring for 24 h. It was then poured into 500 mL of ice water. to afford Pyr HBA 4Br as a brownish solid with an 82 % yield. In a N_2-filled flask, Pyr-HBA-4Br (0.50 g, 0.35 mmol) and paraformaldehyde (0.05 g, 1.66 mmol) were completely dispersed in 80 mL 1,4-dioxane and 20 mL EtOH. The reaction mixture was maintained at 110 °C with continuous stirring for 24 h. The solvents were concentrated under vacuum, and the residue was washed three times with MeOH. The resulting rust color solid was obtained as the Pyr-BZ-4Br monomer [Yield: 71 %]. FTIR [cm^{-1}]: 3036 (sp^2 C—H), 2193 (C≡C), 947 (oxazine). ^1H NMR [500 MHz, ppm, δ, DMSO-d_6]: 8.72, 8.38, 7.67, 7.27, 7.14, 7.10, 7.00, 5.58, and 4.74 ppm. NMR [125 MHz, ppm, δ, DMSO-d_6]: 149.9, 133.1, 131.6, 129.9, 128.7, 126.3, 119.2, 114.1, 113.7, 98.6 (Pyr-C ≡ **C**-Ph) and 85.2 (Pyr-**C** ≡ C-Ph).

2.5. Synthesis of Pyr-BZ-Pyr POP

CuI (1.9 mg), Pyr-BZ-4Br (0.15 g, 0.10 mmol), $Pd(PPh_3)_4$ (11.5 mg), Pyr-T (30.8 mg, 0.10 mmol), and PPh_3 (2.62 mg) were charged into a Pyrex reaction tube. Under a nitrogen atmosphere, anhydrous DMF (10 mL) and Et_3N (10 mL) were introduced, and the tube was closed. The mixture was then subjected to heating at 110 °C with stirring for 72 h to effect the Sonogashira coupling reaction. Once cooled to 25 °C, the crude product was isolated by filtration and washed sequentially with THF and MeOH until the filtrate was clear. The reaction afforded 0.10 g of Pyr-BZ-Pyr POP, which was isolated as a reddish-brown powder. Pyr-BZ-Pyr POP was heated in an oven at 300 °C for 2 h, yielding a dark-brown solid, denoted as poly(Pyr-BZ-Pyr POP). Elemental analysis (EA) indicated that the C, N, and H contents of Pyr-BZ-Pyr POP were 76.32 %, 11.57 %, and 5.24 %, respectively, while poly(Pyr-BZ-Pyr POP) exhibited corresponding values of 77.41 %, 10.26 %, and 5.78 %.

3. Result and discussion

3.1. The synthesis and thermal ring-opening polymerization of Pyr-BZ-4Br monomer

In this work, we first synthesized the Pyr-T-4NH_2 precursor, which features a pyrene portion, alkynyl linkages, and terminal amine functionalities. To construct the benzoxazine monomer Pyr-BZ-4Br, we then implemented a streamlined, three-step sequence including Schiff-base condensation with 4-bromosalicylaldehyde, reductive amination, and Mannich condensation, which has recently gained prominence for its efficiency in assembling multifunctional architectures while obviating labor-intensive purification steps. The use of 4-bromosalicylaldehyde in the initial Schiff-base reaction ensures that each benzoxazine ring incorporates a bromine "handle" at its periphery, thereby facilitating subsequent cross-coupling modifications. The progression from Pyr-T-4NH_2 to Pyr-BZ-4Br is depicted in Fig. 1(a), and the corresponding FTIR spectra, shown in Fig. 1(b), provide clear evidence of each transformation. In the spectrum of Pyr-T-4NH_2, strong absorptions at approximately 3461 and 3363 cm^{-1} arise from asymmetric and symmetric -NH_2 stretching, while the band at 3030 cm^{-1} corresponds to aromatic sp^2 C—H stretching and the peak at 2191 cm^{-1} confirms the presence of C≡C bonds. Following Schiff-base formation, the imine product Pyr-SF-4Br exhibits a new C═N stretch at 1616 cm^{-1} alongside an O—H band near 3425 cm^{-1}, with the alkyne stretch retained at 2192 cm^{-1}. Subsequent reduction to Pyr-HBA-4Br is evidenced by the departure of the imine band and the emergence of N—H and O—H stretches at 3380 and 3417 cm^{-1}, respectively. Finally, ring closure via Mannich condensation to form Pyr-BZ-4Br is confirmed by the loss of

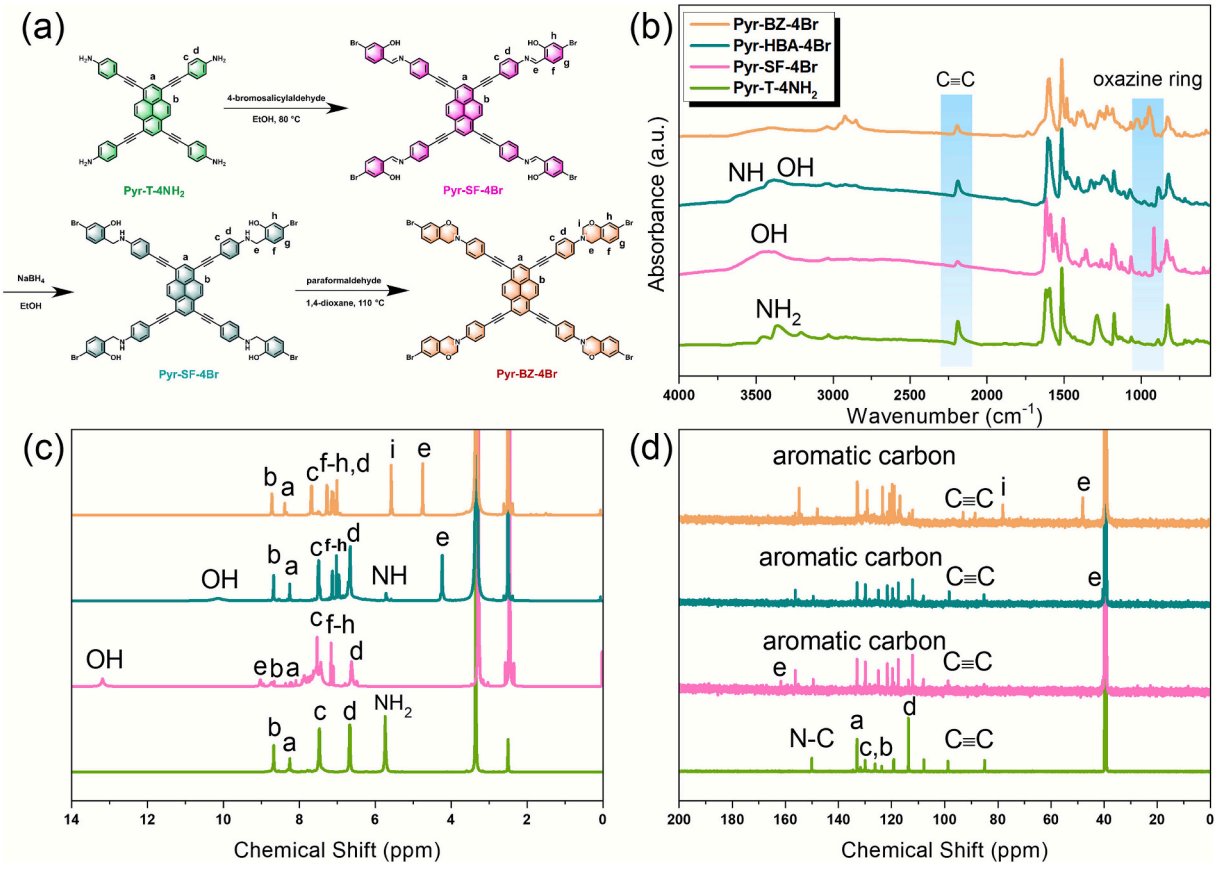

Fig. 1. (a) Three-step synthetic route to Pyr-BZ-4Br monomer. Spectroscopic characterization of each intermediate and the final product: (b) FTIR, (c) ^1H NMR, and (d) ^{13}C NMR spectra of Pyr-T-4NH_2, Pyr-SF-4Br, Pyr-HBA-4Br, and Pyr-BZ-4Br.

both O—H and N—H signals, the persistence of the C≡C and aromatic C—H stretches at 2193 and 3036 cm^{-1}, and the appearance of the characteristic [1,3]-oxazine vibration at 947 cm^{-1}. Together, these spectroscopic data validate the efficient, high-yielding conversion of Pyr-T-4NH_2 into the targeted benzoxazine monomer. The ^{1}H and ^{13}C NMR spectra of each tetraethynylpyrene derivative are presented in Figs. 1(c) and 1(d), respectively, and collectively confirm the stepwise structural transformations. In the spectrum of Pyr-T-4NH_2, the aromatic protons appear as downfield signals at 8.67, 8.25, 7.46, and 6.66 ppm, while the NH_2 protons resonate at 5.73 ppm. The pronounced deshielding of these signals reflects the extended magnetic-field-induced ring-current effects of the pyrene portion [**Scheme S1**].

Post Schiff-base condensation to give Pyr-SF-4Br, solubility limitations broaden the resonances, but distinct peaks can still be identified at 13.18 ppm (phenolic O**H**), 9.02 ppm (**H**C=N), and a cluster of aromatic resonances between 8.65 and 6.63 ppm. Reduction of Pyr-SF-4Br with $NaBH_4$ yielded Pyr-HBA-4Br, as confirmed by the disappearance of the imine resonance at 9.02 ppm and the appearance of a new NH-C**H**$_2$ signal at 4.23 ppm. In addition, aromatic and phenolic OH protons gave rise to multiplets at 10.17, 8.67, 8.25, 7.49, 7.12–7.14 (doublet of doublet), 7.02, 6.95–6.96 (dd), 6.65, 5.71 ppm, consistent with the formation of the secondary amine. With the departure of **H**-C=N, the characteristic peaks of NH-CH_2 appear instead, symbolizing the success of the reduction. Upon Mannich ring closure, the $NHCH_2$ group vanishes and is replaced by two distinct oxazine methylene signals at 5.58 ppm (Ar-C**H**$_2$-N) and 4.74 ppm (O-C**H**$_2$-N). These emerge alongside aromatic proton signals at 8.72, 8.38, 7.67–7.68 (dd), 7.26–7.27 (dd), 7.00 ppm. The near 1:1 integration of the Ar-C**H**$_2$-N and O-C**H**$_2$-N peaks further confirms quantitative formation of the [1,3]-oxazine ring. The ^{13}C NMR spectrum of each intermediate, shown in Fig. 1(d), provides further confirmation of our synthetic sequence. In the spectrum of Pyr-T-4NH_2, resonances at 150 ppm correspond to the Ph-NH_2 carbon, while aromatic carbons appear between 133 and 107 ppm. The alkyne carbons give rise to two distinct signals at 98 and 85 ppm. Following Schiff-base formation, the key imine carbon emerges at 161 ppm in the Pyr-SF-4Br spectrum, alongside aromatic signals spanning 156–108 ppm and the unchanged alkyne resonances at 98 and 85 ppm. Reduction with $NaBH_4$ to yield Pyr-HBA-4Br is evidenced by the departure of the C=N peak, while the aromatic and alkyne carbons remain at 156–108, 98, and 85 ppm; importantly, a new methylene carbon at 40 ppm confirms formation of the NH-CH_2 moiety. Finally, Mannich condensation to form Pyr-BZ-4Br is corroborated by the loss of the NH-CH_2 resonance, the appearance of benzoxazine methylene signals at 48 ppm (Ph-CH_2-N) and 78 ppm (O-CH_2-N), and aromatic peaks between 154 and 112 ppm along with alkyne carbons at 93 and 88 ppm. Together, these ^{13}C shifts definitively demonstrate the successful conversion of Pyr-T-4NH_2 into the target benzoxazine monomer. In light of our structural characterization, we proceeded to investigate the thermal ring-opening polymerization (ROP) behavior of the Pyr-BZ-4Br monomer by differential scanning calorimetry (DSC), Fourier-transform infrared spectroscopy (FTIR), and thermogravimetric analysis (TGA). Upon ROP, the [1,3]-oxazine rings in Pyr-BZ-4Br undergo homolytic cleavage to generate reactive Mannich-type intermediates that link adjacent monomer units into a crosslinked network [Fig. 2(a) and **Scheme S2**].

Concomitantly, newly formed phenolic -OH groups establish extensive hydrogen-bonding interactions, as depicted in Fig. 2(b). To monitor the onset and progression of ring opening, we recorded FTIR spectra after isothermal treatments at temperatures ranging from 25 to 280 °C.

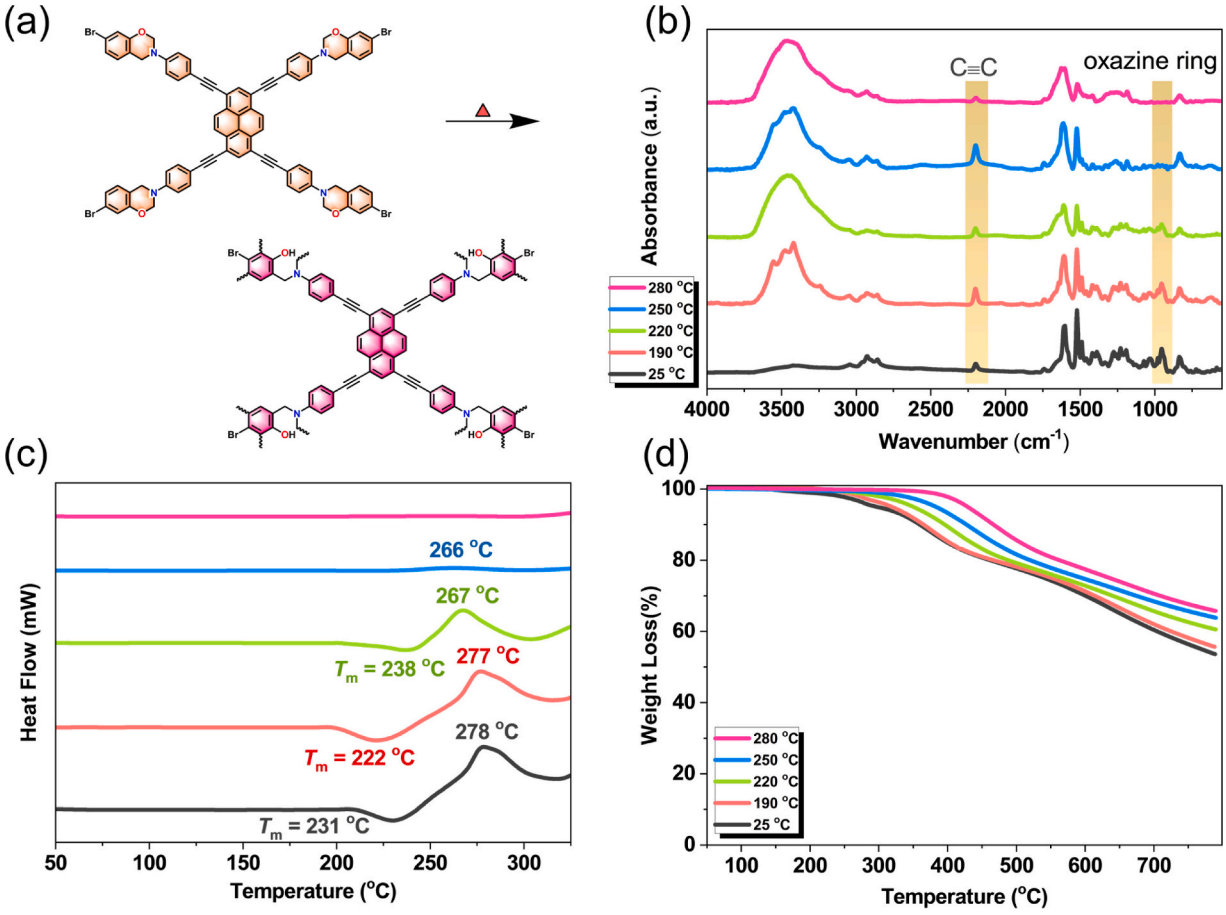

Fig. 2. (a) Proposed molecular structure of Pyr-BZ-4Br after thermal ROP process and the corresponding (b) FTIR spectra, (c) DSC thermograms, and (d) TGA curves of Pyr-BZ-4Br at several temperatures [25–280 °C].

The characteristic [1,3]-oxazine rings vibration at 947 cm^{-1} progressively diminished and was completely absent above 250 °C, while the alkyne stretch at 2191 cm^{-1} remained intact, underscoring the thermal resilience of the C≡C bonds. DSC thermograms of the Pyr-BZ-4Br monomer displayed a melting endotherm (T_m) at 231 °C, followed by a pronounced exothermic peak (T_{exo}) at 278 °C, which we attribute to the exothermic ring-opening and polymerization of the [1,3]-oxazine segments to yield poly(Pyr-BZ-4Br) [Fig. 2(c)]. With the escalating temperature of heat treatment, T_{exo} shifted from 278 °C down to 266 °C before disappearing altogether after treatment at 280 °C, consistent with the completion of ROP. These thermal events are summarized in **Table S1**. Fig. 2(d) displays the TGA analyses of Pyr-BZ-4Br at different temperatures. It can be observed that the thermal decomposition temperature (T_{d10}) and char yield of Pyr-BZ-4Br monomer (T_{d10} = 359 °C, char yield = 53.4 wt%) are obtained without heat treatment. After ROP [190–280 °C], the values of T_{d10} were 364, 396, 427, and 466 °C while the values of char yield were 55.4, 60.3, 63.6, and 65.6 wt%, indicating that the formation of a highly crosslinked poly(Pyr-BZ-4Br) network was shown in Fig. 2(a), as summarized in **Table S1**.

3.2. Synthesis and characterization of Pyr-BZ-Pyr POP

The synthesis of the precursor materials—namely Pyr-T-4NH_2, Pyr-BZ-4Br, and Pyr-T—is straightforward, cost-effective, and affords high yields. These characteristics make the preparation process highly efficient and economically viable. Consequently, both Pyr-BZ-Pyr POP and its polymeric counterpart, poly(Pyr-BZ-Pyr POP), can be readily produced on a large scale, highlighting their strong potential for practical and industrial applications. Upon verification of the structure of Pyr-BZ-4Br monomer and the successful incorporation of its [1,3]-oxazine rings, we synthesized Pyr-BZ-Pyr POP via Sonogashira coupling reaction with Pyr-T. The overall strategy is illustrated in Fig. 3(a). FTIR analysis [Fig. 3 (b)] reveals the departure of the terminal alkyne C—H stretch at 3279 cm^{-1} and the retention of the C≡C and aromatic C—H bands at 2189 and 3054 cm^{-1}, respectively, alongside the characteristic oxazine vibration at 963 cm^{-1}. This observation confirms efficient cross-coupling without disrupting the [1,3]-oxazine rings. Additionally, solution-phase ^{13}C NMR spectra of Pyr-T recorded in $CHCl_3$-*d* and DMSO-d_6 [Fig. 3(c) and **Figs. S1-S3**] show aromatic resonances between 135 and 117 ppm and alkyne carbons at 83 and 81 ppm in $CHCl_3$-*d*, which shift to 88 and 81 ppm in DMSO-d_6 due to hydrogen-bonding interactions [**Scheme S3**]. In contrast, the solid-state ^{13}C NMR spectrum of Pyr-BZ-Pyr POP exhibits signals at 179–118 ppm (aromatic carbons), 97 ppm (C≡C), 81 ppm (O-CH_2-N and C≡C), and 47 ppm (Ph-CH_2-N), demonstrating the incorporation of both monomeric.

motifs into the final network. Finally, optical characterization further validates the structure and photophysical behavior of pyrene derivatives. **Fig. S4** illustrates that X-ray photoelectron spectroscopy (XPS) verified the incorporation of carbon (C), nitrogen (N), and oxygen (O) in the Pyr-BZ-Pyr POP framework, accounting for 43 %, 24 %, and 20 % of the elemental composition, respectively. The high-resolution C 1 s spectrum of Pyr-BZ-Pyr POP was resolved into four distinct components located at 283.8, 284.44, 285.23, and 285.83 eV, which are attributed to C-C/C=C, C≡C, C—O, and C—N bonding environments, respectively [**Fig. S5(a)**]. Similarly, the N 1 s spectrum exhibited a single well-defined peak centered at 399.62 eV, characteristic of C—N linkages

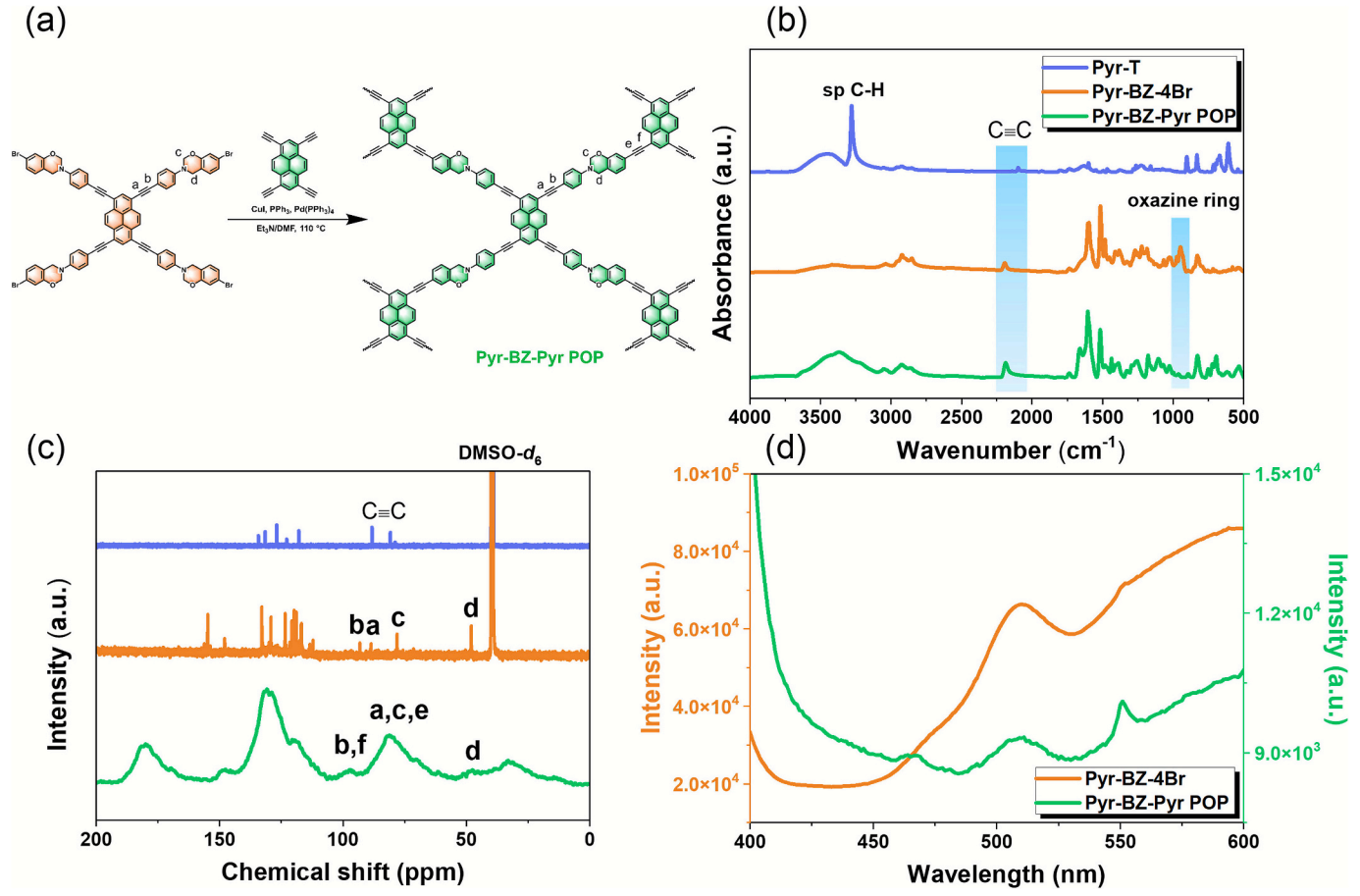

Fig. 3. (a) The synthetic route to the Pyr-BZ-Pyr POP via Sonogashira coupling reaction and the corresponding (b) FTIR spectra of Pyr-T, Pyr-BZ-4Br and Pyr-BZ-Pyr POP, (c) ^{13}C NMR spectra of of Pyr-T, Pyr-BZ-4Br and Pyr-BZ-Pyr POP, and (d) PL profiles of the solid-state of Pyr-BZ-4Br and Pyr-BZ-Pyr POP with an excitation wavelength of 380 nm.

within the framework [**Fig. S5(b)**]. The O 1 s spectrum showed a prominent peak at 532.01 eV, corresponding to C–O–C units [**Fig. S5 (c)**]. A detailed summary of the XPS peak-fitting results for Pyr-BZ-Pyr POP is provided in **Table S2**. UV–Vis spectra of Pyr-BZ-4Br monomer (10^{-5} M in THF) and Pyr-BZ-Pyr POP dispersed in THF both display a π-π* absorption peak at ~380 nm [**Fig. S6**], indicative of the conjugated pyrene-alkyne-benzene structures. Solid-state photoluminescence [Fig. 3(d)] shows that Pyr-BZ-4Br emits at 510 and 551 nm (λ_{exc} = 380 nm), whereas Pyr-BZ-Pyr POP exhibits a new band at 465 nm in addition to peaks at 509 and 551 nm, reflecting the extended conjugation and altered electronic environment within the crosslinked polymer. Together, these spectroscopic data confirm the successful synthesis and functional integration of Pyr-BZ-Pyr POP. To evaluate the photophysical response of both the Pyr-BZ-4Br monomer and its Pyr-BZ-Pyr POP, we recorded their photoluminescence (PL) spectra in THF under 380 nm excitation [Figs. 4(a) and 4(b)]. For the Pyr-BZ-4Br monomer, PL intensity steadily escalated as its concentration was raised from 10^{-8} to 10^{-5} M, culminating in pronounced emission peaks at 531 and 554 nm at the highest concentration. This concentration-dependent enhancement confirms aggregation-induced emission (AIE) behavior, which we attribute to reduced intramolecular motion and the formation of lone-pair-π and π-π aggregates between the [1,3]-oxazine rings and the pyrene moieties [69–71].

In contrast, dispersion of the crosslinked Pyr-BZ-Pyr POP in THF at 5 mg/ mL produced three distinct emission peaks at 411, 435, and 538 nm, corresponding respectively to its conjugated alkyne segments and pyrene chromophores [Fig. 4(b)]. To probe the π-mediated interactions of this polymer network with carbon nanostructures, single-walled carbon nanotubes (SWCNTs) were introduced at incremental loadings. Even at a low loading of 1 wt% SWCNTs, the 538 nm emission band associated with pyrene moieties was sharply quenched, while the alkyne-related peaks at 411 and 435 nm experienced only modest attenuation. Escalating the SWCNTs concentration to 2 wt% resulted in the complete suppression of all photoluminescent bands, suggesting highly efficient energy transfer from both the alkyne and pyrene chromophores to the nanotube scaffold. Furthermore, the SEM images (**Fig. S7**) reveal that the SWCNTs exhibit a filamentous morphology and form a uniform, conformal coating on the surface of Pyr-BZ-Pyr POP. This intimate interfacial contact suggests robust interactions between the components, which are likely to impact the photophysical properties of the composite.

3.3. *Thermal polymerization behavior and morphology of Pyr-BZ-Pyr POP and poly(Pyr-BZ-Pyr POP)*

The thermal curing and stability of the Pyr-BZ-Pyr POP network were evaluated by FTIR, DSC, and TGA, and the results are summarized in Fig. 5 and **Table S3**. Upon ROP to 300 °C, the FTIR spectrum of Pyr-BZ-Pyr POP [Fig. 5(a)] shows complete departure of the oxazine-ring vibration at 963 cm^{-1}, while the alkyne stretch around 2190 cm^{-1} and aromatic C—H band around 3054 cm^{-1} remain unaffected, indicating selective ring-opening polymerization without degradation of the backbone. This interpretation is corroborated by the corresponding DSC thermogram [Fig. 5(b)], where the characteristic exothermic peak associated with ring opening vanishes after curing, signifying full conversion to a crosslinked poly(Pyr-BZ-Pyr POP) network [schematically illustrated in Fig. 5(d)]. **Fig. S4** presents the XPS results, which demonstrate the presence of C, N, and O in the poly(Pyr-BZ-Pyr POP) framework. The corresponding elemental compositions were determined to be 49 % for C, 20 % for N, and 31 % for O. The deconvoluted high-resolution C 1 s spectrum of poly(Pyr-BZ-Pyr POP) displays four well-resolved peaks at binding energies of 283.9, 284.57, 285.62, and 286.42 eV, which are assigned to C–C/C=C, C≡C, C–OH, and C-Nchemical environments, respectively [**Fig. S5(d)**]. Likewise, the N 1 s spectrum consists of a single prominent peak at 399.49 eV, confirming the presence of C—N functionality within the poly(Pyr-BZ-Pyr POP) [**Fig. S5(e)**].

The O 1 s spectrum features a distinct peak at 531.98 eV, corresponding to C–OH functionalities [**Fig. S5(e)**]. A comprehensive summary of the XPS peak-fitting analysis and associated surface functional groups of poly(Pyr-BZ-Pyr POP) is compiled in **Table S2**. In Fig. 5(c), TGA analysis further demonstrates that the Pyr-BZ-4Br, Pyr-BZ-Pyr POP,

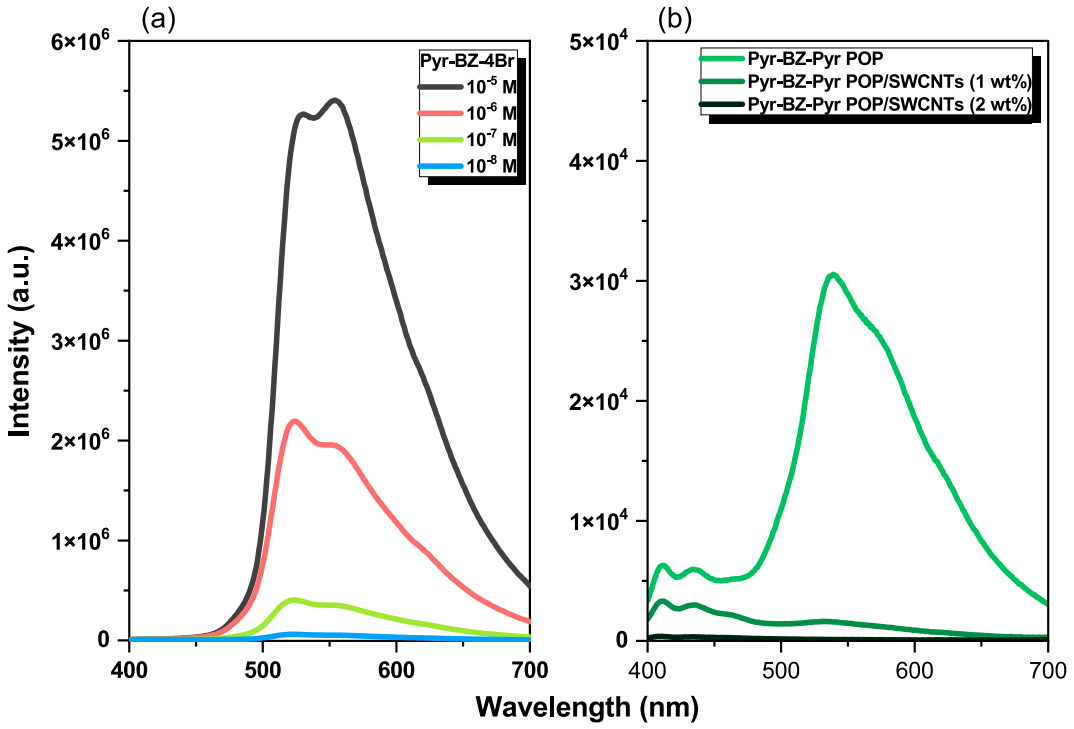

Fig. 4. PL spectra of (a) various concentrations of Pyr-BZ-4Br and (b) Pyr-BZ-Pyr POP and Pyr-BZ-Pyr POP/SWCNTs complex in THF solution with an excitation wavelength of 380 nm.

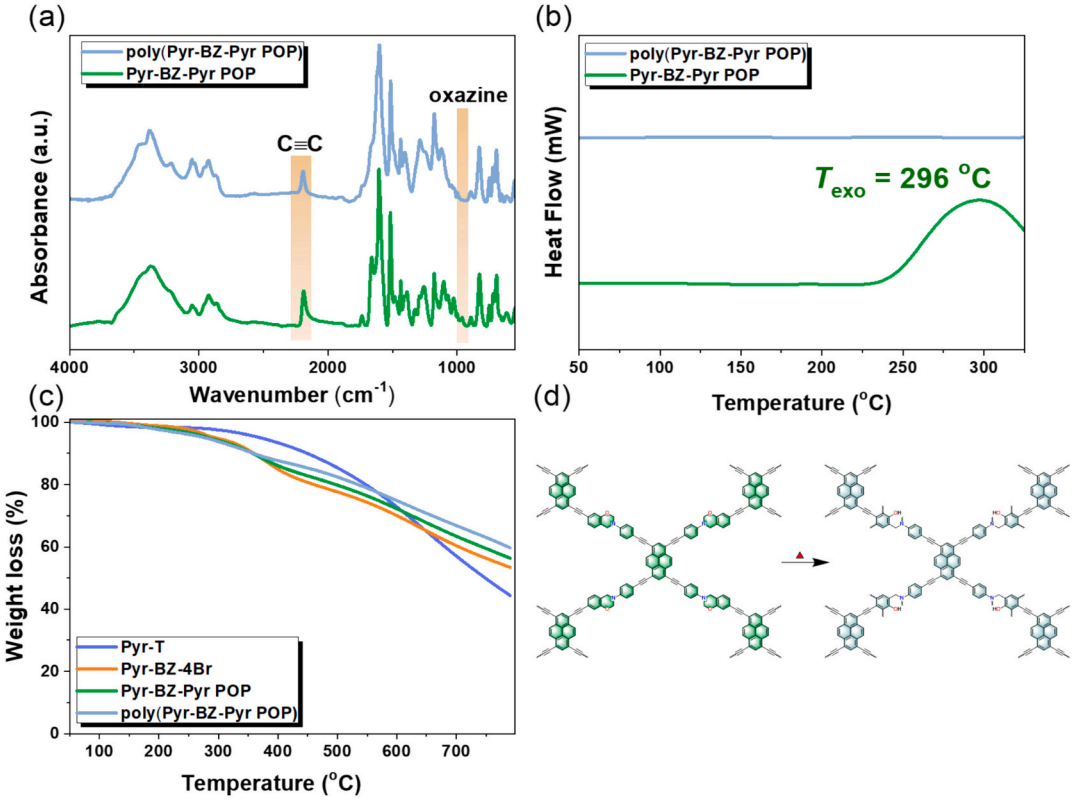

Fig. 5. (a) FTIR spectra and (b) DSC profiles of Pyr-BZ-Pyr POP, and poly(Pyr-BZ-Pyr POP).(c) TGA analysis of Pyr-T, Pyr-BZ-4Br, Pyr-BZ-Pyr POP, and poly(Pyr-BZ-Pyr POP). (d) The possible structure of Pyr-BZ-Pyr POP after the thermal ROP process.

and poly(Pyr-BZ-Pyr POP) networks exhibit high thermal stability, with T_{d10} and residual char yields listed in **Table S3**. While the Pyr-BZ-Pyr POP and its crosslinked poly(Pyr-BZ-Pyr POP) network exhibit comparable T_{d10} values, their thermal performance remains slightly inferior to that of the smaller Pyr-BZ-4Br monomer, which benefits from reduced steric hindrance and closer proximity of benzoxazine units, facilitating more extensive crosslinking. Consequently, Pyr-BZ-4Br achieves higher char yield and decomposition temperatures than its larger Pyr-BZ-Pyr POP counterpart. The surface morphology and porosity characteristics of both Pyr-BZ-Pyr POP and its thermally cured counterpart, poly(Pyr-BZ-Pyr POP), were systematically investigated using nitrogen adsorption-desorption isotherms. As illustrated in Figs. 6(a) and 6(b), both materials exhibit type V isotherms with slight hysteresis loops, suggesting the presence of a hierarchical porous structure composed of both microporous and mesoporous domains. This dual porosity indicates that the materials possess interconnected networks with varying pore sizes, which may enhance their potential for guest molecule uptake. According to the Brunauer–Emmett–Teller (BET) model, the specific surface area of the as-synthesized Pyr-BZ-Pyr POP was measured to be 117 $m^2 g^{-1}$, while that of the crosslinked poly(Pyr-BZ-Pyr POP) network decreased slightly to 89 $m^2 g^{-1}$. Similarly, the total pore volumes were determined to be 0.81 $cm^3 g^{-1}$ and 0.73 $cm^3 g^{-1}$, respectively. This slight reduction in surface area and pore volume after thermal curing is likely attributable to partial pore collapse or network densification resulting from the formation of covalent crosslinks during ring-opening polymerization [72,73]. To gain deeper insight into the pore size distribution, non-local density functional theory (NLDFT) was employed. The results revealed that both materials possess well-defined micropores, with dominant pore sizes centered at approximately 1.4 nm for Pyr-BZ-Pyr POP and 1.9 nm for poly(Pyr-BZ-Pyr POP). This slight expansion of micropores after thermal treatment is attributed to the ring-opening of the [1,3]-oxazine ring, which induces structural rearrangement and increased pore accessibility. In addition to microporosity, mesoporous features were also observed. Pyr-BZ-Pyr POP showed mesopores centered at 2.9 nm and 5.4 nm, while the cured poly (Pyr-BZ-Pyr POP) retained the dominant mesoporous structure at 5.4 nm, as summarized in **Table S4**. These findings confirm that both materials exhibit hierarchical porosity with moderate surface areas, making them promising candidates for applications in gas storage or capture.

The Scanning electron microscopy (SEM) micrograph of Pyr-BZ-Pyr POP [**Fig. S8(a)**] reveals a loosely packed, plate-like architecture punctuated by irregular, cauliflower-shaped aggregates. These features are indicative of a hierarchical, open framework in which micron-sized sheets are interwoven with smaller nodular domains, consistent with the dual micro/mesoporous structure inferred from gas adsorption measurements. Energy-dispersive X-ray (EDS) mapping [**Figs. S8(b)-S8(d)**] confirms that carbon, nitrogen, and oxygen are homogeneously distributed. Following ROP and covalent crosslinking of the [1,3] oxazine segments, the poly(Pyr-BZ-Pyr POP) network adopts a markedly different appearance [**Fig. S9(a)**]: the platelets collapse and fuse into densely packed, sub-micron clusters, leading to a reduction in macroporosity and surface area while preserving intrinsic micro and mesopores at smaller scales. This morphological evolution parallels the modest decrease in BET surface area and pore volume observed after thermal curing, underscoring the structural impact of network formation on pore architecture. SEM-EDS mapping [**Figs. S9(b)–S9(d)**] confirms the homogeneous distribution of carbon, nitrogen, and oxygen elements throughout the poly(Pyr BZ Pyr POP) framework. To evaluate and improve the water stability of Pyr-BZ-Pyr POP and poly(Pyr-BZ-Pyr POP), the authors measured the water contact angles (WCA) of both materials. Interestingly, both Pyr-BZ-Pyr POP and poly(Pyr-BZ-Pyr POP), exhibited high WCA values of up to 125°, as shown in **Fig. S10**, indicating excellent hydrophobicity and water resistance. To assess their suitability for CO_2 capture, CO_2 adsorption isotherms were measured at both 273 K and 298 K [Fig. **6(c)**]. At ambient temperature (298 K), the uncured Pyr-BZ-Pyr POP adsorbs 0.30 mmol g^{-1} of CO_2, whereas the

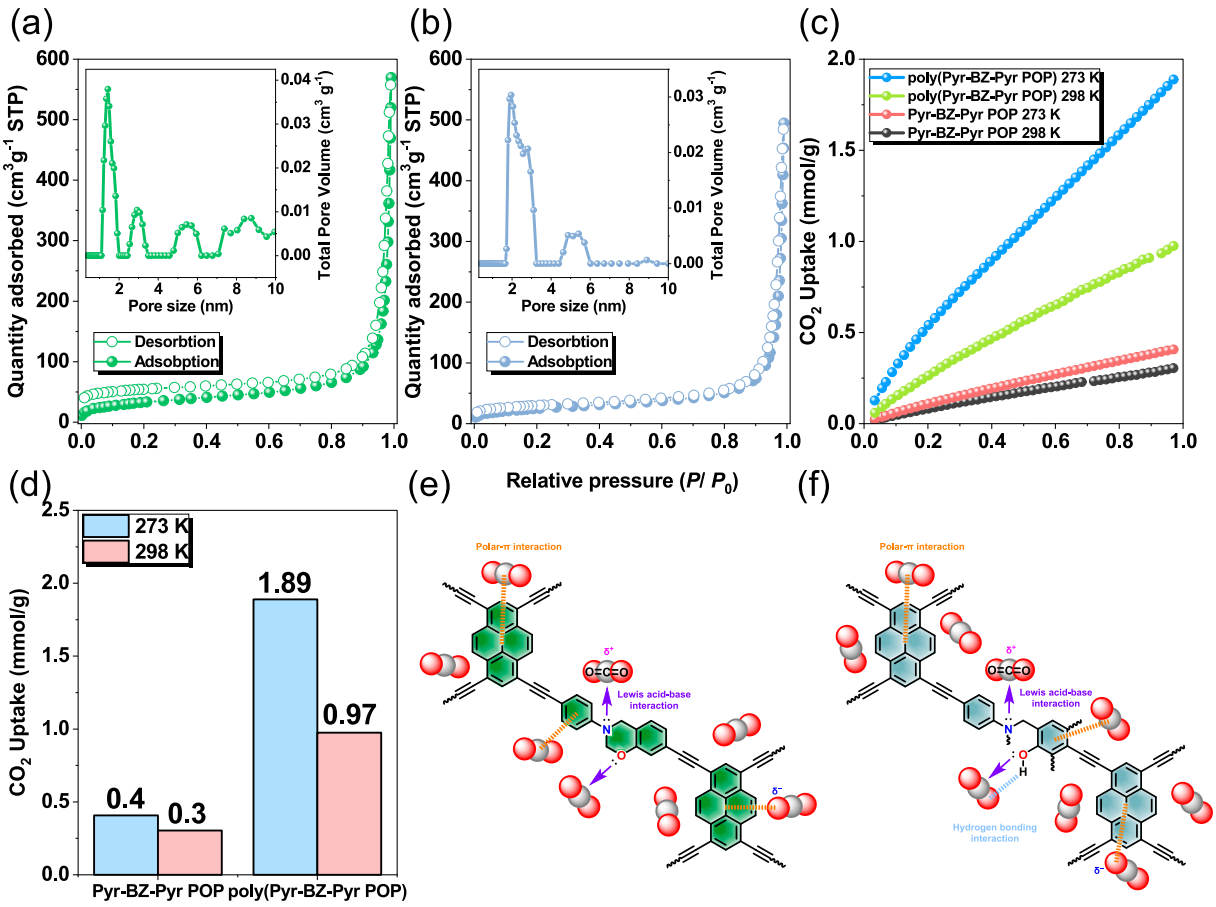

Fig. 6. N_2 adsorption/desorption isotherms and pore size distribution of (a) Pyr-BZ-Pyr POP, and (b) poly(Pyr-BZ-Pyr POP), CO_2 adsorption profiles of Pyr-BZ-Pyr POP and poly(Pyr-BZ-Pyr POP) at 273 and 298 K, and (d) summarize their corresponding CO_2 uptake and schematic illustrations of the proposed CO_2 capture mechanisms in (e) Pyr-BZ-Pyr POP and (f) poly(Pyr-BZ-Pyr POP).

cured poly(Pyr-BZ-Pyr POP) captures 0.97 mmol g^{-1}. At 273 K, these values escalated to 0.3 mmol g^{-1} and 1.89 mmol g^{-1}, respectively. The corresponding isosteric heats of adsorption (Q_{st}) are 29.1 kJ mol^{-1} for Pyr-BZ-Pyr POP and 52.7 kJ mol^{-1} for poly(Pyr-BZ-Pyr POP), indicating stronger binding interactions in the thermally crosslinked framework. [Fig. 6(d) **and Table S4**]. This inversion in adsorption capacity underscores the primacy of pore-size tuning and specific host-guest interactions over simple BET metrics. The Pyr-BZ-Pyr POP framework is able to capture CO_2 through a combination of polar-π interactions between the electron-rich pyrene units and the CO_2 quadrupole, Lewis acid-base interactions involving the oxazine nitrogen and carbon dioxide, and dipole-quadrupole interactions arising from the intrinsic polarity of the [1,3]-oxazine segment, as illustrated in Fig. 6(e). Upon thermal ROP reaction to form poly(Pyr-BZ-Pyr POP), the newly generated phenolic -OH groups further enhance CO_2 affinity by hydrogen-bonding to the oxygen atoms of CO_2 [8], as shown in Fig. 6(f). FTIR analyses [**Figs. S11 and S12**] show that the characteristic absorptions of both Pyr-BZ-Pyr POP and poly(Pyr-BZ-Pyr POP) are retained after CO_2 adsorption. Although the surface area and total pore volume of the network decrease slightly after curing, these hydrogen-bonding interactions act to confine CO_2 more effectively within the remaining pore structure. As a result, poly(Pyr-BZ-Pyr POP) exhibits superior CO_2 uptake despite its lower BET parameters, underscoring the importance of specific host–guest interactions in dictating gas-capture performance. The N_2 adsorption capacities of poly(Pyr-BZ-Pyr POP) were evaluated at 298 and 273 K, as depicted in **Figs. S13(a) and S13(b)**. The measured N_2 uptake values were determined to be 0.09 mmol g^{-1} at 298 K and 0.25 mmol g^{-1} at 273 K, respectively. The CO_2/N_2 selectivity was determined from the initial linear regions of the gas adsorption isotherms at low pressures (≤ 0.14 bar) at both 298 and 273 K, employing Henry's law constants derived from the corresponding slopes [**Figs. S13(c) and S13(d)**]. Based on this analysis, poly(Pyr-BZ-Pyr POP) exhibited a CO_2/N_2 selectivity of 6.1 at 298 K, which increased to 7.6 at 273 K. The cyclic stability test of poly(Pyr-BZ-Pyr POP) for CO_2 uptake (five consecutive adsorption-cycles at 273 K; Figs. 7(a) and 7(b) reveals a decrease in capacity from 1.89 to 1.36 mmol g^{-1}, corresponding to approximately 72 % retention of the initial uptake. This indicates moderate recyclability of the material under the tested conditions. Moreover, compared with many previously reported POP and COF materials, both Pyr-BZ-Pyr POP and poly(Pyr-BZ-Pyr POP) exhibit relatively moderate CO_2 adsorption capacities at 298 and 273 K. [Figs. 7(c) and 7(d) and **Table S5**] [17,25,55,65–67].

Fig. S14 illustrates the molecular electrostatic potential (MESP) map of the monomeric unit of poly(Pyr-BZ-Pyr POP), revealing distinct regions with varying electrostatic potential. The map clearly shows a region of high charge density localized around the -OH group, indicating a strong tendency for selective interaction with the carbon atom of CO_2 through combined electrostatic attraction and hydrogen-bonding effects. In contrast, the highly electron-deficient region appears near the nitrogen (—N) atom adjacent to the -OH group, depicted as the blue area in the MESP map. Because this nitrogen is a tertiary center, its lone pair is delocalized within the polymeric framework, making it less reactive toward the electrophilic carbon of CO_2. Additionally, the aromatic rings display moderately negative potential, suggesting their possible role as secondary adsorption sites for CO_2. Overall, the -OH region exhibits the strongest affinity toward CO_2; therefore, subsequent analyses primarily focus on this site to gain deeper mechanistic insight. **Fig. S15** depicts the spatial distributions of the highest occupied molecular orbital (HOMO)

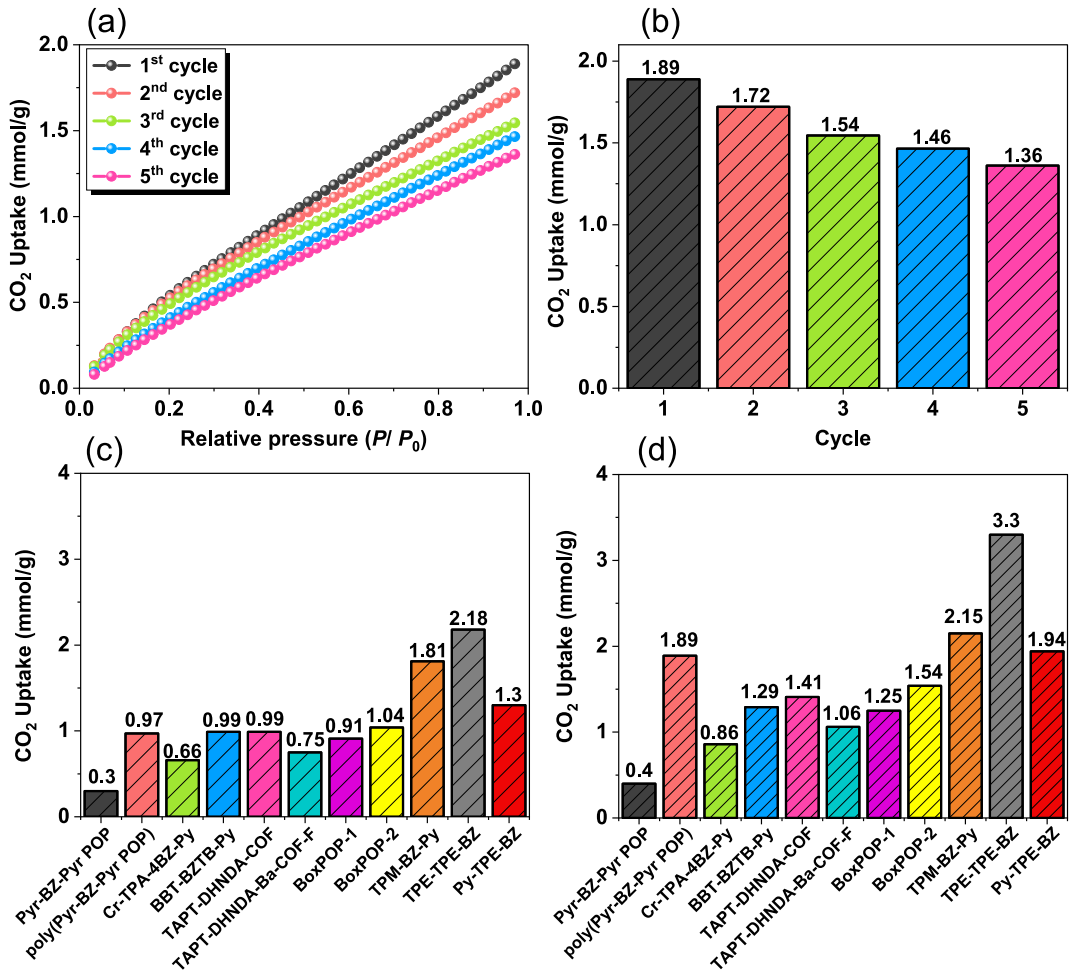

Fig. 7. (a) Repeated CO_2 adsorption cycles of poly(Pyr-BZ-Pyr POP) measured at 273 K, and (b) a summary of the corresponding CO_2 uptake values for each cycle. (c, d) The CO_2 uptake capacity of poly(Pyr-BZ-Pyr POP) at (c) 298 K and (d) 273 K is presented alongside comparative data from other reported COF and POP materials.

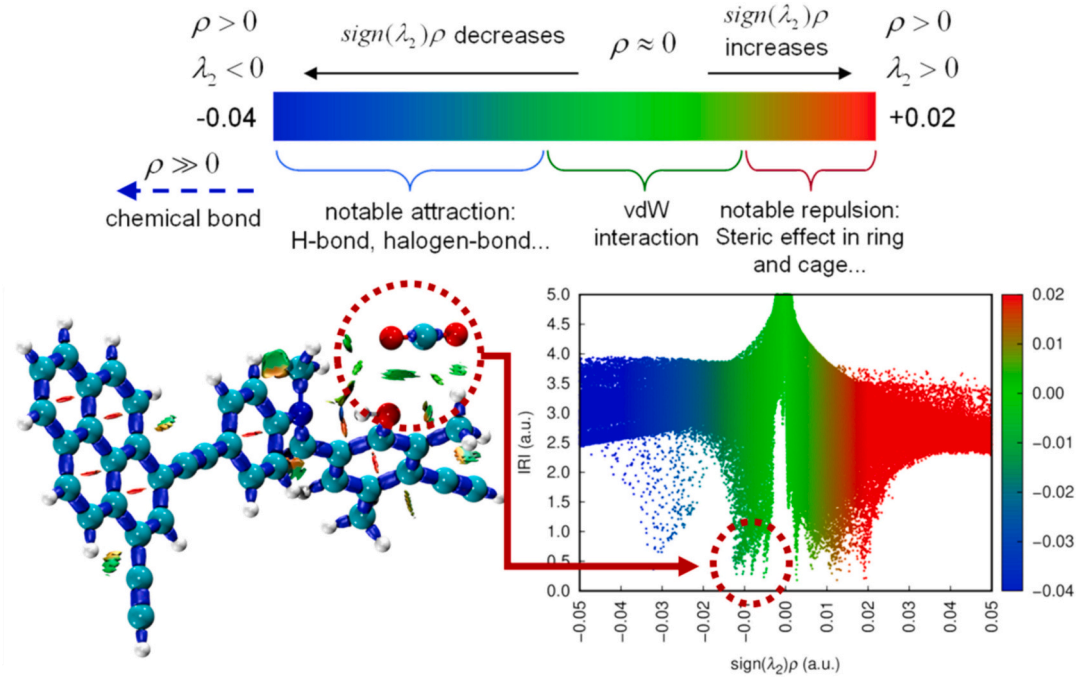

Fig. 8. The 3D isosurfaces and 2D scatter graphs of poly(Pyr-BZ-Pyr POP)@CO_2 complex.

and lowest unoccupied molecular orbital (LUMO) for both pristine poly (Pyr-BZ-Pyr POP) and its CO_2-adsorbed complex, hereafter referred to as poly(Pyr-BZ-Pyr POP)@CO_2 complex. The calculated band gap for the Pyr-BZ-Pyr POP is 2.37 eV, which slightly increases to 2.42 eV upon CO_2 adsorption. This minor shift indicates minimal electronic perturbation, suggesting that the interaction between CO_2 and the poly(Pyr-BZ-Pyr POP) is primarily physisorptive in nature. In the poly(Pyr-BZ-Pyr POP) @CO_2 complex, the HOMO is uniformly delocalized across the aromatic framework, reflecting efficient charge distribution along the poly(Pyr-BZ-Pyr POP) backbone. In contrast, the HOMO of the pristine poly (Pyr-BZ-Pyr POP) is mainly localized around the -OH group, consistent with the high charge density observed in the MESP map (**Fig. S14**). Importantly, CO_2 adsorption does not cause any substantial change in the overall HOMO–LUMO distribution, further corroborating the dominance of physical rather than chemical adsorption in this system.

Investigating non-covalent interactions is crucial for elucidating the adsorption mechanism, and the Interaction Region Indicator (IRI) serves as an effective tool for visualizing and characterizing these weak forces. To analyze such interactions, two-dimensional scatter plots of the reduced density gradient (RDG) versus λ_2, along with three-dimensional isosurfaces, were generated for the poly(Pyr-BZ-Pyr POP)@CO_2 complex, as shown in Fig. 8. Distinct green isosurfaces are observed between the poly(Pyr-BZ-Pyr POP) framework and the CO_2 molecule, indicating the presence of weak non-covalent interactions involving oxygen atoms and the aromatic units of the poly(Pyr-BZ-Pyr POP). Specifically, the oxygen atoms of CO_2 form interactions with the -CH_2 groups attached to the tertiary-N centers of the poly(Pyr-BZ-Pyr POP), while additional C—O and C—C contacts are established between CO_2 and the delocalized π-electron cloud of the aromatic core. These combined interactions contribute to electrostatic stabilization, consistent with the trends predicted by the HOMO–LUMO orbital analysis. Moreover, the RDG scatter plot exhibits characteristic peaks within the range of 0.0 to −0.01 a.u., confirming the existence of weak non-covalent interactions, as highlighted in Fig. 8.

4. Conclusions

A convergent synthetic strategy was developed to access a Pyr-BZ-4Br monomer and its crosslinked porous organic polymer (Pyr-BZ-Pyr POP) through sequential Schiff-base condensation, reductive amination, Mannich condensation, and Sonogashira coupling. The Pyr-BZ-4Br exhibited excellent thermal stability with a T_{d10} of 359 °C and a char yield of 53.4 wt%. After ROP at 280 °C, these values increased to 466 °C and 65.6 wt%, respectively, indicating the formation of a highly crosslinked network. Notably, CO_2 uptake improved significantly after thermal curing, reaching 1.89 mmol g^{-1} at 273 K, compared to 0.40 mmol g^{-1} before curing [Pyr-BZ-Pyr POP]. Notably, the poly(Pyr-BZ-Pyr POP) displayed superior CO_2 adsorption capacity, despite a modest loss in surface area, underscoring the decisive role of pore-size tuning, phenolic -OH binding sites, and Mannich bridges can serve as active binding sites capable of establishing strong intermolecular hydrogen bonding with CO_2 molecules, thereby improving the material's capacity for CO_2 adsorption. This study demonstrates that the resulting poly(Pyr-BZ-Pyr POP) exhibits promising potential for gas capture applications. Future research will focus on incorporating alternative heteroatoms and precisely tuning the pore architecture of the poly(Pyr-BZ-Pyr POP) framework to enhance its performance in separation technologies, dye adsorption, and photocatalytic applications.

CRediT authorship contribution statement

Mohamed Gamal Mohamed: Writing – review & editing, Writing – original draft, Supervision, Methodology, Investigation, Formal analysis, Data curation, Conceptualization. **Yang-Chin Kao:** Investigation, Data curation, Conceptualization. **Bo-Xuan Su:** Data curation, Conceptualization. **Hira Karim:** Software. **Shiao-Wei Kuo:** Supervision, Resources.

Declaration of competing interest

The authors declare that they have no known competing financial interests or personal relationships that could have appeared to influence the work reported in this paper.

Acknowledgments

This study was supported financially by the National Science and Technology Council, Taiwan, under contracts NSTC 114-2223-E-110-001- and 113-2221-E-110-012-MY3. The authors thank the staff at National Sun Yat-sen University for their assistance with the TEM (ID: EM022600) experiments.

Appendix A. Supplementary data

Supplementary data to this article can be found online at https://doi.org/10.1016/j.seppur.2025.136692.

Data availability

The data that has been used is confidential.

References

[1] M. Filonchyk, M.P. Peterson, L. Zhang, V. Hurynovich, Y. He, Greenhouse gases emissions and global climate change: examining the influence of CO_2, CH_4, and N_2O, Sci. Total Environ. 935 (2024) 173359, https://doi.org/10.1016/j.scitotenv.2024.173359.

[2] L. Wang, Y. Ma, H. Liu, Y. Guo, B. Yang, B. Chang, Leveraging porosity and morphology in hierarchically porous carbon microtubes for CO_2 capture and separation from humid flue gases, Sep. Purif. Technol. 354 (2025) 128910, https://doi.org/10.1016/j.seppur.2024.128910.

[3] Y. Dai, Z. Niu, Y. Wang, S. Zhong, P. Mu, J. Li, Recent advances and prospect of emerging microporous membranes for high-performance CO_2 capture, Sep. Purif. Technol. 318 (2023) 123992, https://doi.org/10.1016/j.seppur.2023.123992.

[4] S.O. Akpasi, I.M.S. Anekwe, E.K. Tetteh, U.O. Amune, S.I. Mustapha, S.L. Kiambi, Hydrogen as a clean energy carrier: advancements, challenges, and its role in a sustainable energy future, Clean Energy 9 (2025) 52–88, https://doi.org/10.1093/ce/zkae112.

[5] E. Sivasurya, R. Atchudan, M.G. Mohamed, A. Thangamani, S. Rajendran, A. Jalil, P.K. Kalambate, D. Manoj, S.W. Kuo, Electrocatalytic conversion of CO_2 into selective carbonaceous fuels using metal-organic frameworks: An overview of recent progress and perspectives, Mater. Today Chem. 44 (2025) 102538, https://doi.org/10.1016/j.mtchem.2025.102538.

[6] X. Tian, C. An, Z. Chen, The role of clean energy in achieving decarbonization of electricity generation, transportation, and heating sectors by 2050: A meta-analysis review, Renew. Sust. Energ. 182 (2023) 113404, https://doi.org/10.1016/j.rser.2023.113404.

[7] W. Shi, Y. Guo, Q. Lu, H. Li, Y. Liang, F. Ma, B. Yang, B. Chang, Dynamic tailoring of the gradient porosity of biomass-derived porous carbons for highly effective CO_2 capture, Green Chem. 27 (2025) 11416–11428, https://doi.org/10.1039/D5GC03217B.

[8] X. Gao, S. Yang, L. Hu, S. Cai, L. Wu, S. Kawi, Carbonaceous materials as adsorbents for CO_2 capture: synthesis and modification, Carbon Capture Sci. Technol. 3 (2022) 100039, https://doi.org/10.1016/j.ccst.2022.100039.

[9] M. Alizadeh, Y. Khalili, M. Ahmadi, Comprehensive review of carbon capture and storage integration in hydrogen production: opportunities, challenges, and future perspectives, Energies 17 (2024) 5330, https://doi.org/10.3390/en17215330.

[10] F. Raganati, P. Ammendola, CO_2 post-combustion capture: a critical review of current technologies and future directions, Energy Fuel 38 (2024) 13858–13905, https://doi.org/10.1021/acs.energyfuels.4c02513.

[11] Y. Wang, L. Huang, S. Li, C. Liu, H. He, The capture and catalytic conversion of CO_2 by dendritic mesoporous silica-based nanoparticles, Energy Environ. Mater. 7 (2024) e12593, https://doi.org/10.1002/eem2.12593.

[12] M. Tan, X. Li, Y. Feng, B. Wang, L. Han, W. Bao, L. Chang, J. Wang, Fly ash-derived mesoporous silica with large pore volume for augmented CO_2 capture, Fuel 351 (2023) 128874, https://doi.org/10.1016/j.fuel.2023.128874.

[13] A.M. Najafi, S. Soltanali, H. Ghassabzadeh, Enhancing the CO_2, CH_4, and N_2 adsorption and kinetic performance on FAU zeolites for CO_2 capture from flue gas by metal incorporation technique, J. Chem. Eng. 468 (2023) 143719, https://doi.org/10.1016/j.cej.2023.143719.

[14] C. Cammarere, J. Cortés, T.G. Glover, R.Q. Snurr, J.T. Hupp, J. Liu, Water-enhanced CO_2 capture in metal-organic frameworks, Front. Chem. 13 (2025) 1634637, https://doi.org/10.3389/fchem.2025.1634637.

[15] S. Das, P. Sharma, M. Kumar, R.K. Gupta, H. Sharma, A review on clay exfoliation methods and modifications for CO_2 capture application, Mater. Today Sustain. 23 (2023) 100427, https://doi.org/10.1016/j.mtsust.2023.100427.
[16] T. Li, X. An, D. Fu, Review on nitrogen-doped porous carbon materials for CO_2 adsorption and separation: recent advances and outlook, Energy Fuel 37 (2023) 8160–8179, https://doi.org/10.1021/acs.energyfuels.3c00941.
[17] M.G. Mohamed, C.C. Chen, K. Zhang, S.W. Kuo, Construction of three-dimensional porous organic polymers with enhanced CO_2 uptake performance via solid-state thermal conversion from tetrahedral benzoxazine-linked precursor, Eur. Polym. J. 200 (2023) 112551, https://doi.org/10.1016/j.eurpolymj.2023.112551.
[18] M. Ejaz, M.G. Mohamed, S.W. Kuo, Benzoxazine-linked polyhedral oligomeric silsesquioxane: 3D porous organic-inorganic polymer for improved CO_2 capture and supercapacitor performance, J. Taiwan Inst. Chem. Eng. (2025) 106098, https://doi.org/10.1039/D3PY00158J.
[19] A.K. Maharana, S.K. Sarkar, S. Mukherjee, R. Sarkar, G. Rambabu, K. Sugamata, S. Das, Triazole-boosted dual-structured covalent triazine frameworks for ultra-stable high-energy and-power density aqueous supercapacitors and notable selective CO_2 capture, J. Mater. Chem. A 13 (2025) 11717–11731, https://doi.org/10.1039/D5TA01351H.
[20] Y.C. Kao, K.T. Yeh, M.G. Mohamed, H. Karim, W.H. Su, S.W. Kuo, Structural modulation via mesoporous silica templating in covalent organic frameworks: converting functional aspects for adsorption behavior, Sep. Purif. Technol. 357 (2025) 133827, https://doi.org/10.1016/j.seppur.2025.133827.
[21] M.G. Mohamed, C.C. Chen, M. Ibrahim, A.O. Mousa, M.H. Elsayed, Y. Ye, S.W. Kuo, Tetraphenylanthraquinone and dihydroxybenzene-tethered conjugated microporous polymer for enhanced CO_2 uptake and supercapacitive energy storage, JACS Au 4 (2024) 3593–3605, https://doi.org/10.1021/jacsau.4c00537.
[22] M.G. Mohamed, S.Y. Chang, M. Ejaz, M.M. Samy, A.O. Mousa, S.W. Kuo, Design and synthesis of bisulfone-linked two-dimensional conjugated microporous polymers for CO_2 adsorption and energy storage, Molecules 28 (2023) 3234, https://doi.org/10.3390/molecules28073234.
[23] Q. Liao, Y. Yuan, J. Cao, One-step synthesis of hydroxyl-functionalized ionic hyper-cross-linked polymers with high surface areas for efficient CO_2 capture and fixation, J. Colloid Interface Sci. 665 (2024) 958–968, https://doi.org/10.1016/j.jcis.2024.03.185.
[24] M.G. Mohamed, A.F.M. EL-Mahdy, M.G. Kotp, S.W. Kuo, Advances in porous organic polymers: syntheses, structures, and diverse applications, Mater. Adv. 3 (2022) 707–733, https://doi.org/10.1039/D1MA00771H.
[25] M.G. Mohamed, C.C. Chen, S.W. Kuo, Nitrogen and sulfur co-doped microporous carbon through benzo[c]-1,2,5-thiadiazole-functionalized benzoxazine-linkage porous organic polymer in CO_2 capture and energy storage, React. Funct. Polym. 214 (2025) 106286, https://doi.org/10.1016/j.reactfunctpolym.2025.106286.
[26] H. Amasha, A. Ahmad, I. Abdulazeez, O. Charles, S. Al Hamouz, Microwave-synthesized heteroaromatic porous organic polymers for CO_2 capture and hydrogen, Mater. Today Sustain. 27 (2024) 100879, https://doi.org/10.1016/j.mtsust.2024.100879.
[27] B. Chang, W. Shi, H. Yin, S. Zhang, B. Yang, Poplar catkin-derived self-templated synthesis of N-doped hierarchical porous carbon microtubes for effective CO_2 capture, Chem. Eng. J. 358 (2019) 1507–1518, https://doi.org/10.1016/j.cej.2018.10.142.
[28] M. Goto, T. Yajima, M. Minami, H. Sogawa, F. Sanda, Synthesis and cross-linking of a benzoxazine-containing anthracene moiety: thermally stable photoluminescent benzoxazine resin, Macromolecules 53 (2020) 6640–6648, https://doi.org/10.1021/acs.macromol.0c00910.
[29] L. Xie, R. Yang, N. Li, P. Froimowicz, K. Zhang, Competitive study of novel triptycene-containing benzoxazine monomers and a thermoresponsive linear main chain-type benzoxazine copolymer: synthesis, polymerization, and thermal properties of their thermosets, Macromolecules 55 (2022) 6973–6981, https://doi.org/10.1021/acs.macromol.2c00853.
[30] D. Trybuła, A.M. Harych, M. Gazińska, S. Berski, D. Jędrzkiewicz, J. Ejfler, N-activated 1,3-benzoxazine monomer as a key agent in Polybenzoxazine synthesis, Macromolecules 53 (2020) 8202–8215, https://doi.org/10.1021/acs.macromol.0c02036.
[31] R. Yang, K. Zhang, Design and synthesis of flavonoid-based mono-, bis-, and tri-benzoxazines: toward elucidating roles of oxazine ring number and hydrogen bonding on their polymerization mechanisms and thermal properties, Macromolecules 58 (2025) 616–626, https://doi.org/10.1021/acs.macromol.4c02616.
[32] R. Yang, Q. Chen, W. Sheng, K. Zhang, Oxazine ring-containing polycyclic monomers: a class of benzoxazine thermosetting resins with intrinsically low curing temperature, Macromolecules 57 (2024) 5608–5619, https://doi.org/10.1021/acs.macromol.4c00829.
[33] S. Mukherjee, S. Sahu, B. Lochab, Elucidating the role of conjugated alkenyl functionalities at the oxazine ring in governing the polymerization mechanism of 4th generation-biobased benzoxazine thermosets, Macromolecules 57 (2024) 5200–5207, https://doi.org/10.1021/acs.macromol.4c00458.
[34] S. Mukherjee, B. Lochab, Hydrogen bonding-guided strategies for thermal performance modulation in biobased oxazine ring-substituted benzoxazine thermosets, Macromolecules 57 (2024) 1795–1807, https://doi.org/10.1021/acs.macromol.3c02454.
[35] T.L. Ma, W.T. Du, Y.C. Kao, M.G. Mohamed, S.W. Kuo, Reaction-induced miscibility in styrene-and benzoxazine-based copolymers with poly (vinylpyrrolidone) blends through strong intermolecular hydrogen-bonding interactions, Macromolecules 58 (2025) 6215–6227, https://doi.org/10.1021/acs.macromol.5c00004.
[36] N. Li, S. Yang, K. Zhang, Thiophene-rich benzoxazines with an amide moiety: integration of structural and hydrogen bonding influence on the polymerization mechanism by experimental and computational studies, Macromolecules 56 (2023) 6667–6678, https://doi.org/10.1021/acs.macromol.3c01515.
[37] J. Liu, L. Zhang, X. Zhu, Q. Chen, K. Zhang, X. Liu, Design of a low-temperature ring-opening benzoxazine system using a supramolecular hydrogen-bond structure, ACS Appl. Polym. Mater. 5 (2023) 6595–6606, https://doi.org/10.1021/acsapm.3c01107.
[38] V. Duhan, B. Lochab, Glyoxal-based bi-oxazine benzoxazines: formaldehyde-free biothermosets, Macromolecules 57 (2024) 10812–10823, https://doi.org/10.1021/acs.macromol.4c01358.
[39] M. Zeng, H. Luo, Z. Feng, N. He, C. Tang, J. Chen, D. Zeng, Y. Zhou, Y. Shen, Structural design and polymerization of high-frequency low dielectric benzoxazine resins, ACS Appl. Polym. Mater. 6 (2024) 6614–6626, https://doi.org/10.1021/acsapm.4c00891.
[40] C. Hu, Z. Yao, W. Zhao, K. Zhang, Synthesis, characterization, and structure–property investigations of benzoxazine resins with low surface free energy, Macromol. Chem. Phys. 226 (2025) 2400152, https://doi.org/10.1002/macp.202400152.
[41] Y.C. Kao, Y.H. Ku, M.G. Mohamed, W.H. Su, S.W. Kuo, Microphase separation transformation in bio-based benzoxazine/phenolic/PEO-*b*-PCL diblock copolymer mixtures induced by transesterification reaction, Macromolecules 58 (2025) 585–600, https://doi.org/10.1021/acs.macromol.4c02072.
[42] R. Yang, N. Li, C.J. Evans, S. Yang, K. Zhang, Phosphaphenanthrene-functionalized benzoxazines bearing intramolecularly hydrogen-bonded phenolic hydroxyl: synthesis, structural characterization, polymerization mechanism, and property investigation, Macromolecules 56 (2023) 1311–1323, https://doi.org/10.1021/acs.macromol.3c00028.
[43] Y.C. Kao, M.G. Mohamed, P.H. Chen, A.A. Thabet, A.A.K. Mohammed, S.W. Kuo, Characterization and polymerization kinetics of triazine-based benzoxazine monomers: effects of pyridine and bromine interactions, ACS Appl. Polym. Mater. 7 (2025) 10212–10223, https://doi.org/10.1021/acsapm.5c02017.
[44] M. Stępień, E. Nizioł, M. Gazińska, A.M. Harych, W. Zierkiewicz, L. John, P. Wytrych, J. Ejfler, Polymerization case with Hydroxybenzoxazines: what is the role of the hydroxy group, does it act as a self-catalyst or a modifier of the polymer structure? Macromolecules 58 (2024) 473–487, https://doi.org/10.1021/acs.macromol.4c01664.
[45] Z. Yang, Z. Xie, Y. Zhang, H. Chen, Z. Tang, X.L. Sha, Fully bio-based benzoxazine adhesive with enhanced strength via synergistic supramolecular and covalent cross-linking, ACS Appl. Polym. Mater. 6 (2024) 12897–12905, https://doi.org/10.1021/acsapm.4c02842.
[46] M.G. Mohamed, S.W. Kuo, Crown ether-functionalized Polybenzoxazine for metal ion adsorption, Macromolecules 53 (2020) 2420–2429, https://doi.org/10.1021/acs.macromol.9b02519.
[47] E.A. Gorbunova, V.V. Shutov, I.S. Sirotin, Polymerization scheme and chemical structure of aromatic diamine-based Polybenzoxazines: new details, Macromol. Chem. Phys. 225 (2024) 2400119, https://doi.org/10.1002/macp.202400119.
[48] L. Pursche, A. Wolf, T. Urbaniak, K. Koschek, Benzoxazine/amine-based polymer networks featuring stress-relaxation and reprocessability, Front. Soft Matter. 3 (2023) 1197868, https://doi.org/10.3389/frsfm.2023.1197868.
[49] T. Uramatsu, S. Morinaga, T. Shibatsuka, T. Kawauchi, Polymer alloys with high thermal properties consisting of polyfunctional benzoxazine derived from an oligonuclear phenolic compound and bismaleimide, Polym. J. 56 (2024) 1223–1230, https://doi.org/10.1038/s41428-024-00947-0.
[50] Z. Tang, Y. Tan, H. Chen, Y. Wan, Benzoxazine: A privileged scaffold in medicinal chemistry, Curr. Med. Chem. 30 (2023) 372–389, https://doi.org/10.2174/0929867329666220705140846.
[51] R. Malekkhouyan, M.G. Olivier, A review on the application of benzoxazine as coatings and corrosion inhibitors for corrosion protection of metallic substrates, Mater. Today Chem. 45 (2025) 102614, https://doi.org/10.1016/j.mtchem.2025.102614.
[52] Y. Lu, J. Liu, W. Zhao, K. Zhang, Bio-benzoxazine structural design strategy toward highly thermally stable and intrinsically flame-retardant thermosets, J. Chem. Eng. 457 (2023) 141232, https://doi.org/10.1016/j.cej.2022.141232.
[53] I. Chatterjee, K. Ali, G. Panda, A synthetic overview of benzoxazines and benzoxazepines as anticancer agents, ChemMedChem 18 (2023) e202200617, https://doi.org/10.1002/cmdc.202200617.
[54] Y.C. Kao, J.Y. Lin, W.C. Chen, M.G. Mohamed, C.F. Huang, J.H. Chen, S.W. Kuo, High-thermal stable epoxy resin through blending nanoarchitectonics with double-decker-shaped polyhedral silsesquioxane-functionalized benzoxazine derivatives, Polymers 16 (2023) 112, https://doi.org/10.3390/polym16010112.
[55] M.G. Mohamed, B.X. Su, S.W. Kuo, Robust nitrogen-doped microporous carbon via crown ether-functionalized benzoxazine-linked porous organic polymers for enhanced CO_2 adsorption and supercapacitor applications, ACS Appl. Mater. Interfaces 16 (2024) 40858–40872, https://doi.org/10.1021/acsami.4c05645.
[56] M. Ejaz, M.G. Mohamed, S.W. Kuo, Fluorescent benzoxazine–perylene linked covalent organic polymer as a sensing probe for lead ions and 2,4,6-trinitrophenol, ACS Appl. Polym. Mater. 6 (2024) 9170–9179, https://doi.org/10.1021/acsapm.4c01514.
[57] H.W. Chen, M.G. Mohamed, Y.C. Kao, W.C. Chen, K. Chiou, S.W. Kuo, Overcoming synthetic challenges in developing high-performance polybenzoxazine from diamine-functionalized double-Decker silsesquioxane (DDSQ) cage, Eur. Polym. J. 232 (2025) 113929, https://doi.org/10.1016/j.eurpolymj.2025.113929.
[58] M. Ejaz, M.G. Mohamed, Y.T. Chen, K. Zhang, S.W. Kuo, Porous carbon materials augmented with heteroatoms derived from hyperbranched biobased benzoxazine

resins for enhanced CO_2 adsorption and exceptional supercapacitor performance, J. Energy Storage 78 (2024) 110166, https://doi.org/10.1016/j.est.2023.110166.
[59] C.Y. Chen, W.C. Chen, M.G. Mohamed, Z.Y. Chen, S.W. Kuo, Highly thermally stable, reversible, and flexible main chain type benzoxazine hybrid incorporating both polydimethylsiloxane and double-decker shaped polyhedral silsesquioxane units through diels–alder reaction, Macromol. Rapid Commun. 44 (2023) 2200910, https://doi.org/10.1002/marc.202200910.
[60] Y. Lu, N. Li, Y. Peng, M.G. Mohamed, S.W. Kuo, K. Zhang, Facile and eco-friendly synthesis of hydrogen bonding-rich bio-based bisbenzoxazine resins with low surface free energy, strong adhesion strength and high thermal stability, Mol. Syst. Des. Eng. 9 (2024) 86–98, https://doi.org/10.1039/D3ME00066D.
[61] P.J. Waller, Y.S. Alfaraj, C.S. Diercks, N.N. Jarenwattananon, O.M. Yaghi, Conversion of imine to oxazole and thiazole linkages in covalent organic frameworks, J. Am. Chem. Soc. 140 (2018) 9099–9103, https://doi.org/10.1021/jacs.8b05830.
[62] H. Liu, J. Chu, Z. Yin, X. Cai, L. Zhuang, H. Deng, Covalent organic frameworks linked by amine bonding for concerted electrochemical reduction of CO_2, Chem 4 (2018) 1696–1709, https://doi.org/10.1016/j.chempr.2018.05.003.
[63] F. Haase, E. Troschke, G. Savasci, T. Banerjee, V. Duppel, S. Dorfler, M.M. Grundei, Burow C. Ochsenfeld, S. Kaskel, B.V. Lotsch, Topochemical conversion of an imine-into A thiazole-linked covalent organic framework enabling real structure analysis, Nat. Commun. 9 (2018) 2600, https://doi.org/10.1038/s41467-018-04979-y.
[64] C. Zhao, H. Lyu, Z. Ji, C. Zhu, O.M. Yaghi, Ester-linked crystalline covalent organic frameworks, J. Am. Chem. Soc. 142 (2020) 14450–14454, https://doi.org/10.1021/jacs.0c07015.
[65] M.G. Mohamed, T.C. Chen, S.W. Kuo, Solid-state chemical transformations to enhance gas capture in benzoxazine-linked conjugated microporous polymers, Macromolecules 54 (2021) 5866–5877, https://doi.org/10.1021/acs.macromol.1c00736.
[66] S. Xu, J. He, S. Jin, B. Tan, Heteroatom-rich porous organic polymers constructed by benzoxazine linkage with high carbon dioxide adsorption affinity, J. Colloid Interface Sci. 509 (2018) 457–462, https://doi.org/10.1016/j.jcis.2017.09.009.
[67] Q. Ma, X. Liu, H. Wang, Q. Zhuang, J. Qian, Construction of novel benzoxazine-linked covalent organic framework with antimicrobial activity via postsynthetic cyclization, Mater. Today Chem. 23 (2020) 100707, https://doi.org/10.1016/j.mtchem.2021.100707.
[68] T. Mondal, M.G. Mohamed, A.A.K. Mohamed, S.W. Kuo, Construction of metal-coordinated bipyridine-based conjugated microporous polymers as robust electrocatalysts for hydrogen evolution, ACS Appl. Energy Mater. 8 (2025) 7703–7713, https://doi.org/10.1021/acsaem.5c00992.
[69] M.G. Mohamed, A. Basit, C.Y. Shih, S.U. Sharma, T. Mondal, S.W. Kuo, Pyrene-linked covalent organic polymer/single-walled carbon nanotubes hybrids as high-performance electrodes for Supercapacitive energy storage, ACS Appl. Energy Mater. 8 (2025) 3764–3778, https://doi.org/10.1021/acsaem.5c00052.
[70] M.G. Mohamed, K.C. Hsu, S.W. Kuo, Bifunctional polybenzoxazine nanocomposites containing photo-crosslinkable coumarin units and pyrene units capable of dispersing single-walled carbon nanotubes, Polym. Chem. 6 (2015) 2423–2433, https://doi.org/10.1039/C5PY00035A.
[71] H.K. Shih, C.C. Hsieh, M.G. Mohamed, C.Y. Zhu, S.W. Kuo, Ternary polybenzoxazine/POSS/SWCNT hybrid nanocomposites stabilized through supramolecular interactions, Soft Matter 12 (2016) 1847–1858, https://doi.org/10.1039/C5SM02569A.
[72] C.W. Hsiao, M.G. Mohamed, S.W. Kuo, Structural design and functionalization of benzoxazine-modified octavinylsilsesquioxane hybrid porous polymer through Sonogashira coupling reaction, Mater. Today Chem. 46 (2025) 102795, https://doi.org/10.1016/j.mtchem.2025.102795.
[73] M.G. Mohamed, W.C. Chang, S.W. Kuo, Crown ether- and benzoxazine-linked porous organic polymers displaying enhanced metal ion and CO_2 capture through solid-state chemical transformation, Macromolecules 55 (2022) 7879–7892, https://doi.org/10.1021/acs.macromol.2c01216.